Molecular Crystals and Liquid Crystals
Publication details, including instructions for authors and subscription information:
http://www.tandfonline.com/loi/gmcl20

Cellulose Nanocrystal Reinforced Alginate Fibers—Biomimicry Meets Polymer Processing

Esteban E. Ureña-Benavides [a] & Christopher L. Kitchens [a]
[a] Department of Chemical and Biomolecular Engineering, Clemson University, Clemson, South Carolina, 29634

Available online: 02 Mar 2012

To cite this article: Esteban E. Ureña-Benavides & Christopher L. Kitchens (2012): Cellulose Nanocrystal Reinforced Alginate Fibers—Biomimicry Meets Polymer Processing, Molecular Crystals and Liquid Crystals, 556:1, 275-287

To link to this article: http://dx.doi.org/10.1080/15421406.2012.635977

Mol. Cryst. Liq. Cryst., Vol. 556: pp. 275–287, 2012

ISSN: 1542-1406 print/1563-5287 online
DOI: 10.1080/15421406.2012.635977

Taylor & Francis
Taylor & Francis Group

Cellulose Nanocrystal Reinforced Alginate Fibers—Biomimicry Meets Polymer Processing

ESTEBAN E. UREÑA-BENAVIDES
AND CHRISTOPHER L. KITCHENS*

Department of Chemical and Biomolecular Engineering, Clemson University, Clemson, South Carolina 29634

This research takes a biomimetic approach to the design of polymer nanocomposites and demonstrates structure-property relationships that are controllable via processing conditions. Cellulose nanocrystals (CNCs) measuring 130 nm (length) × 20.4 nm (width) × 6.8 nm (height) were isolated from cotton by sulfuric acid hydrolysis and were incorporated in an alginate fiber wet spinning dope solution. Incorporating CNCs within the alginate fiber enables a nearly two-fold increase in the apparent jet stretch (J_A), ratio of the linear draw speed to extrusion velocity. Fiber spinning at a constant J_A resulted in an unexpected decrease in fiber modulus and increase in toughness. Alternatively, fiber spinning at the maximum J_A resulted in modulus increases that are predicted by the Halpin-Tsai model and the Hui-Shia model. Wide-angle X-ray diffraction (WAXD) was used to elucidate the structure and orientation of cellulose nanocrystals (CNC) within the alginate nanocomposite fibers and provide correlations with mechanical property enhancements. The spread of the azimuthal intensity distribution of the CNC (2,0,0) reflection increased with higher CNC loads until the nanoparticles within the matrix spiraled around the longitudinal axis. The appearance of a spiral angle with increasing CNC load resulted in a step reduction in modulus and increase in toughness. Increased fiber stretching during spinning retarded the appearance of the spiral assembly and increased CNC alignment. This spiral orientation is also observed in native cellulose fibers as a microfibril angle and is deterministic of their mechanical properties.

Keywords Alginate; biomimetic nanocomposites; cellulose nanocrystals; chiral nematic; liquid crystal; nanocomposite fiber

Introduction

The primary distinction of nanotechnology lies in the fact that many materials possess unique properties when their dimensions are restricted to less than 100 nanometers in length. These properties run the whole gamut of the materials world, from unique catalytic or optical properties to extremely high strength to weight ratio composites. The motivation of this work is to understand the nanoscale phenomena that control these properties and develop new synthesis and processing methodologies that lead to new advanced materials [1,2].

*Address correspondence to Christopher L. Kitchens, Department of Chemical and Biomolecular Engineering, Clemson University, Clemson, South Carolina 29634. Phone: (864) 656-2131. E-mail: ckitche@clemson.edu.

Cellulose is the most abundant biopolymer on the planet and is a renewable, strong, lightweight, biocompatible, chemically robust material. Cellulose has been used on an industrial scale in a myriad of materials for more than 150 years, predating polymer fibers by nearly a century [3,4]. Cellulose is the primary skeletal component of plants, providing structural integrity of the primary and secondary plant cell walls and the structural component in tunicate marine animals [5]. It also provides distinctive iridescence that arises from the structural orientation of nanocrystals in fish scales, peacock feathers, butterfly wings and beetle exoskeletons [6–9]. Each of these remarkable properties are the result of nature's bottom up nanoscale assembly of nanocrystalline regions of cellulose within a biomass matrix; nature's own nanocomposite [3].

Expanding upon the structure – property relationships for plant fibers, the secondary cell wall of wood fiber consists of three layers (S1, S2, S3) that wrap around the fiber axis. Each of these layers is composed of cellulose microfibrils that contain crystalline cellulose and possesses a different orientation with respect to the fiber direction. The difference in orientation from the fiber direction is referred to as the microfibril angle (MFA) [10]. Of the three layers, the S2 layer is predominant and typically has the steepest pitch around the fiber axis, MFA $< 30^\circ$, however, this number varies significantly for different species and even within a single plant. The outer S1 and inner S3 layers are much thinner, if existent at all, and posses MFA's that are closer to the normal of the fiber direction, MFA $\sim 80^\circ$ [5,10]. In general, the MFA of a wood fiber refers to the S2 layer and differences in the MFA have profound effects on the wood properties, especially strength and flexibility. A high MFA is typically found in juvenile wood fiber which requires flexibility to withstand battering winds and other environmental exposures. Mature wood fiber possesses a low MFA and is stronger to support the weight of the tree. The MFA has also been observed to increase with the height of a tree. Furthermore, within a single tree branch, tension wood on the upper side of a branch has a low MFA while compression wood on the lower side of a branch has a high MFA. Tension wood also tends to have a more predominant S2 layer and nonexistent S3 layer when compared to compression wood [10].

Similar structure – property relationships also exist in other plant fibers. The crystalline cellulose components of bast fibers (jute, hemp, flax, ramie) are highly aligned and have a low MFA ($\sim 4^\circ$–5°) with respect to the fiber axis. Cotton, on the other hand, has a higher MFA ($\sim 18^\circ$) [5]. As a result, bast fibers have a high tensile modulus compared to cotton, which has a higher elongation at break. Jute fibers have a modulus of 26.5 GPa and 1.5–1.8% elongation at break while cotton has a modulus of 5.5–12.6 GPa and 7.0–8.0% elongation at break [11].

These relationships between the natural fiber mechanical properties and the nanoscale structural orientation of cellulose crystals, is of significant interest from a polymer nanocomposite processing standpoint because it lends opportunity to control fiber mechanical properties by tailoring the self-assembly of nanoparticles within the polymer matrix. We have recently demonstrated the appearance of this structure-property relationship in CNC reinforced alginate fibers. By controlling the CNC weight fraction loading and the fiber wet-spinning properties, we can tailor the mechanical properties which correlate directly with the CNC spiral angle within the alginate fiber.

Alginate fibers have found many applications such as dressings to treat exuding wounds, drug delivery, enzyme immobilization, etc.; however enormous potential in the biomedical field exists if the limited mechanical properties can be overcome without compromising biocompatibility. To this end, cellulose nanocrystals (CNCs) were isolated from cotton and introduced into calcium alginate fibers with the goal of improving their strength and

modulus. The CNCs were mixed with an aqueous sodium alginate dope solution, and wet spun into a $CaCl_2$ bath to form fibers [1]. Alginate fiber wet spinning traditionally involves extruding an aqueous solution of sodium alginate through a spinneret into a water bath containing 5 to 10% salt with a multivalent cation, such as calcium chloride. The divalent cation displaces the sodium within the alginate polymer and effectively cross links the alginate chains to form the fiber. The fibers are continuously drawn onto a take-up roller and dried to remove solvent. When the apparent jet stretch, J_A, (ratio of the fiber take-up draw velocity to spinneret extrusion velocity) is kept constant, addition of the nanocrystals reduces the tensile strength and modulus of the material; however a small concentration of CNCs in the dope solution increases the toughness and enables an increase in the fiber spinning J_A by nearly two fold: at 16.7 vol.% CNC loading the maximum $J_A = 4.6$, as compared to a maximum of 2.4 for the pure alginate fibers. Mechanical testing showed a 38% increase in tenacity and a 123% increase in tensile modulus with 6.1 vol.% CNC loading and $J_A = 4.2$.

Wide angle X-ray diffraction (WAXD) was used to determine the structure and orientation of CNCs within the alginate nanocomposite fibers and provide correlations with the resulting mechanical property enhancements [2]. The orientation of the CNC was determined from the azimuthal intensity distribution of the (2,0,0) reflection where the spread of the orientations increased with higher loads until the nanoparticles spiraled around the fiber axis. Increased fiber stretching retarded the appearance of a spiral assembly and increased CNC alignment. A reduction of tenacity and modulus, and an increase in elongation at break and tensile energy to break (toughness) coincided with the observation of the spiral orientation. These trends are analogous to those found in natural fiber and demonstrate our biomimetic design of CNC nanocomposite fibers.

Experimental

Cellulose nanocrystals where isolated using methods similar to those in the literature [12–14]. In short, Whatman cellulose filter aid was digested by 64 wt% sulfuric acid at 45°C for 50 min; 17.5 ml of acid was used for every gram of cellulose. The reaction was quenched by a 10-fold dilution with cold deionized water. The remaining solids were allowed to precipitate overnight and were separated from the supernatant liquid by decantation. The resultant slurry was dialyzed against deionized water for several days to remove excess acid, low molecular weight carbohydrates formed during hydrolysis, and other water-soluble impurities; fresh DI water was provided daily until a constant pH of 5.5. The CNC dispersion was then ultrasonicated in an ice bath to disperse the CNCs and then filtered to remove any metal particles released from the sonicating horn. The sonication was performed for a total of 35 minutes divided in five segments of seven minutes and a waiting period of two minutes between sonications; the output power was approximately 120 W. The CNCs were then diluted/concentrated to obtain desired concentrations for the phase behavior measurements and blending with alginate solutions. The macroscopic phase separation was studied by placing a sample solution of varying CNC and alginate concentrations in a 1 mm path length cuvette and allowing the sample to settle for at least 3 days. Images of the samples were taken in ambient light and between polarizing films with parallel and perpendicular (crossed) orientations. Polarized light microscopy was also used to study the microstrucuture of the suspensions and dried films. Triaxial dimensions of the CNCs were determined using a Veeco Bioscope atomic force microscope (AFM) in

tapping mode with a 1 nm diameter MikroMasch tip. One drop of a 0.01 wt% CNC solution was dried on a freshly cleaved mica surface and was kept in a vacuum oven overnight before analysis.

Experimental details of the alginate wet spinning process can be found in previous literature [1]. Briefly, high-viscosity sodium alginate (98.4% purity) from the seaweed *Macrocystis pyrifera* (kelp) was purchased from MP Biomedicals, LLC (catalog number 154723) and used as received. Sodium alginate and CNCs dissolved in DI water were mixed to obtain a total alginate concentration of 1.0 wt% and CNCs concentrations to yield CNCs loads in the final fiber of 1.2, 3.1, 6.3, 16.7, and 37.5 vol.%. A metering pump was used to pump the dope solution at 4.5 cm^3/min through a 10-hole spinneret (400 μm diameter each hole) into a 5% w/v $CaCl_2$ coagulating bath. The fiber was drawn through the coagulation bath and wound on a Teflon tube with threads on the outer surface to maintain a tense yarn, control take-up linear velocity, and prevent self-adhesion. The Teflon tube with drawn fiber was then transferred to a second 5% w/v $CaCl_2$ bath and kept there for 2 h to saturate the fiber with Ca^{2+} ions. During the wet spinning process the divalent Ca^{2+} ion displaces the monovalent sodium ion within the alginate polymer and induces ionic cross linking of the alginate fibers to form the fiber. The fiber was then washed with deionized water to remove excess salt, dehydrated in an acetone bath overnight, and let dry; all these steps were carried out at room temperature. The apparent jet stretch, J_A, (ratio of linear take-up velocity to extrusion velocity) was varied from 2.0 to 4.6, depending on the stretching capacity of the fiber, by controlling the take-up linear velocity and maintaining a constant extrusion velocity.

The fibers were conditioned at 65 $\pm$ 2% relative humidity and 21 $\pm$ 1°C for 24 hours prior to tensile testing, which was performed on an INSTRON 5582 using ASTM D2256-02 (2008) standard test method. A total of 21 randomly selected 30 mm long segments from a single yarn were used to determine the fiber modulus, tenacity, and energy to break. Wide-angle X-ray diffraction (WAXD) measurements were performed on the fiber X-ray system in the Center for Advanced Engineered Fibers and Films at Clemson University and are detailed in previous literature [2]. Briefly, a 0.154 nm wavelength (λ) CuKα_1 X-ray beam was used to irradiate an oriented fiber bundle. The WAXD patterns were recorded on a Fujifilm BAS-IP MS2325 image plate located 112 mm from the sample. The patterns were corrected for air scattering and cosmic background, followed by a Fraser correction to convert the blackening densities and pixel positions to intensities and reciprocal space coordinates [15].

The WAXD intensities at twice the Bragg angle (2θ), were averaged with respect to the azimuthal angle (ϕ) and normalized to the intensity at $2\theta = 54^\circ$ to obtain a one dimensional diffraction pattern for each sample. The cellulose and alginate diffraction peaks were deconvoluted in each section by fitting the profile to multiple Lorentzian peaks. The intensity of the primary (2,0,0) diffraction peak for cellulose Iβ at $2\theta = 22.9^\circ$ was used to quantify the degree of orientation of the CNCs within the fiber. The resolved intensity distributions, $I(\phi)$, of the (2,0,0) cellulose reflection for each fiber were fit to two Lorentzian peaks of equal widths (w_i) and areas, with center positions separated by twice the spiral angel (2ψ).

Results and Discussion

Cellulose nanocrystals isolated from cotton and other lignocellulose sources by sulfuric acid hydrolysis are known to form lyotropic chiral nematic or cholesteric liquid crystal phases in aqueous dispersions [13,16,17]. For this study, CNCs were isolated by sulfuric acid hydrolysis and possessed a triaxial geometry of 130 $\pm$ 63 nm in length, 20.4 $\pm$ 7.8 nm

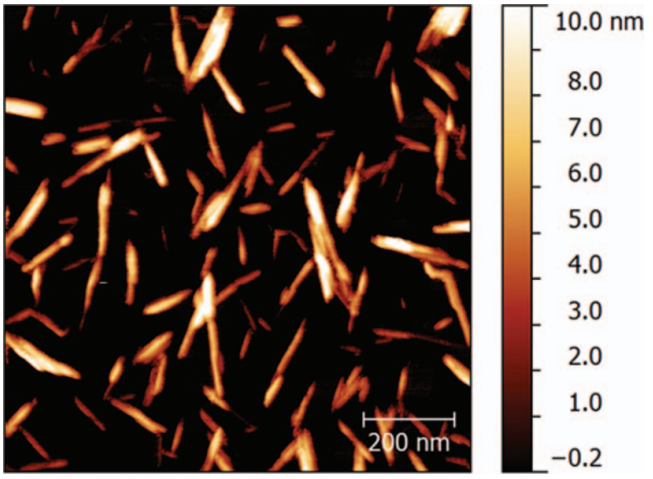

Figure 1. Atomic force microscopy image of cellulose nanocrystals dried on a mica surface. The CNCs were measured to be 130 ± 63 nm in length, 20.4 ± 7.8 nm in width, and 6.8 ± 3.3 nm in height.

in width, and 6.8 ± 3.3 nm in height as measured by AFM [1]. Figure 1 is a representative AFM image of the CNCs and it should be noted that the size distribution analysis included only CNCs that were independent and did not exist as an agglomeration that likely formed during sample preparation. These measurements were confirmed by static light scattering [18]. Figure 2 displays the macroscopic and microscopic visualization of the cholesteric liquid crystalline phase behavior at a CNC concentration of 9.5 wt% in water. At dilute concentrations, below 4.5 wt%, the CNCs are randomly oriented in an isotropic phase, while above this concentration a biphasic region exists that also consists of an ordered anisotropic phase. The volume fraction of the lyotropic cholesteric liquid crystal phase increases with increasing CNC concentration until an upper critical concentration is reached, in which the system exists as a single cholesteric phase. The phase distinction can be readily observed as a dark phase through parallel polarized lenses and a bright phase through

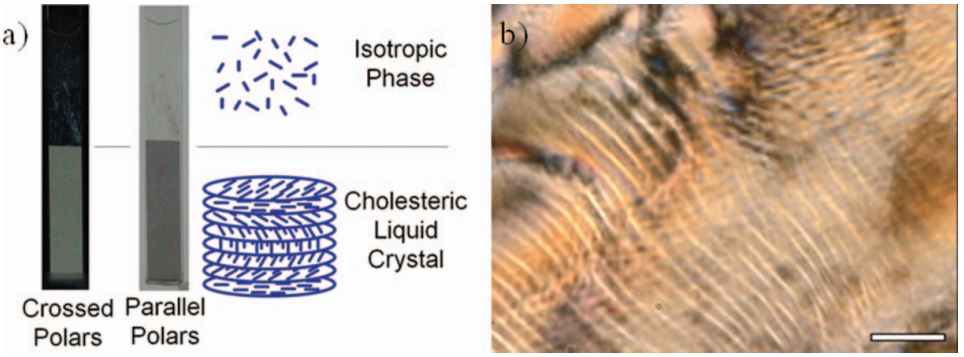

Figure 2. Polarized light imaging. a) Macroscopic phase separation in an aqueous suspension of 0.095 g/ml of CNC. b) Polarized microscopy image of a CNC dried film. The fingerprint texture is indicative of cholesteric liquid crystal; scale bar corresponds to 50 μm.

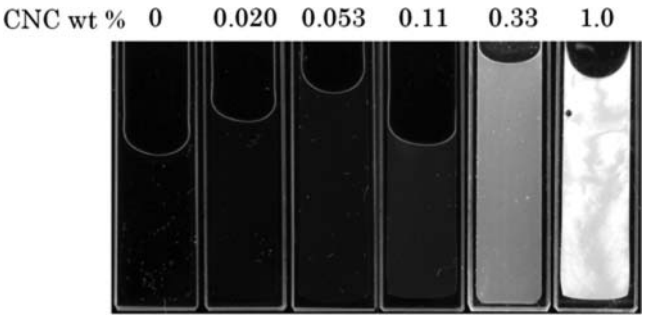

Figure 3. Aqueous solutions containing 1 wt% sodium alginate with varying concentrations of CNCs contained in 1 mm path length cuvettes and imaged between crossed polarizers. From left to right, the samples contain increasing CNC concentrations that yielded fibers with CNC volume fractions of 0.0, 0.012, 0.031, 0.063, 0.167, and 0.375.

cross polarized lenses. The cholesteric phase can also be observed with polarized light microscopy. Figure 2b is an image of a film prepared by drying a CNC suspension on a microscope slide. The fingerprint texture is characteristic of the cholesteric ordering. The same texture is observed if the anisotropic liquid sample is imaged before drying.

Addition of CNCs to 1 wt% aqueous solutions of high viscosity sodium alginate induces liquid crystalline order at lower CNC concentrations as observed in Fig. 3. The phase behavior of rigid rod dispersions, such as CNC, can be altered with the addition of ionic species or other flexible polymers. Gray and co-workers have demonstrated a shift of the isotropic to biphasic critical concentration, C_i, to lower concentrations with the addition of salts and dextrans [16,19,20] Fig. 3 demonstrates that the addition of CNCs to an alginate polymer solution induces liquid crystalline order at CNC weight fractions well below C_i for the CNC dispersion. Biphasic behavior and a distinctive phase transition is not evident with macroscale visualization, however viewing the CNC – alginate dispersion through crossed polarizers provides clear evidence of birefringence and suggests CNC induced order within the alginate polymer chains. When the CNC – alginate solutions are dried into a film and imaged between crossed polarizers, birefringent and non birefringent domains are visible, indicating that the sample contains isotropic and liquid crystal regions. The fraction of liquid crystal regions increases with CNC concentration and is most evident above 6.3 vol.% (10 wt.%). At the highest CNC concentration, 37.5 vol.% (50 wt.%), a fingerprint texture begins to be visualized, suggesting the presence of a chiral nematic order. These results for the solutions and dried films suggest that above a CNC volume fraction of 0.063 with respect to alginate polymer, longer range order exists that may result in the formation of a percolation network within the resulting fiber composite [21,22].

CNC – alginate nanocomposite fibers were produced by wet spinning a 1.0 wt.% alginate dope solution with varying CNC concentrations into a 5% w/v $CaCl_2$ coagulating bath. The solutions, visualized in Fig. 3, contained 0.0, 0.02, 0.053, 0.11, 0.33, and 1.0 wt.% CNC and yielded CNC loads in the resulting composite fibers of 0.0, 1.2, 3.1, 6.3, 16.7, and 37.5 volume percent respectively. Table 1 presents the tensile properties of the nanocomposite fibers. For the sodium alginate and spinneret used in this work, the maximum apparent jet stretch, J_A, of the pure alginate fiber was 2.4; J_A is defined as the ratio of the linear velocity of the uptake roller to the extrusion velocity. First examination of the nanocomposite tensile properties for a constant J_A indicates a decrease in modulus with the addition of CNCs at low loadings and then an increase in modulus at high loadings.

Table 1. Tensile properties and spiral angle determined from the cellulose WAXD (2,0,0) reflection for CNC – alginate nanocomposite fibers. Data reproduced from [2]

	At $J_A = 2.4$				At Max J_A				
CNC Load (vol.%)	Modulus (gpd)	Tenacity $\times 10^2$ (gpd)	Toughness $\times 10^2$ (gpd)	Spiral Angle $\psi(^\circ)$	Max. J_A	Modulus (gpd)	Tenacity $\times 10^2$ (gpd)	Toughness $\times 10^2$ (gpd)	Spiral Angle $\psi(^\circ)$
0	3.1 ± 0.1	14.9 ± 0.4	3.3 ± 0.2	—	2.4	3.1 ± 0.1	14.9 ± 0.4	3.3 ± 0.2	—
1.2	2.6 ± 0.1	15.2 ± 0.5	3.9 ± 0.1	0	3.4	3.8 ± 0.2	18.0 ± 0.7	3.6 ± 0.2	0
3.1	2.8 ± 0.1	14.4 ± 0.3	3.7 ± 0.1	3.6 ± 0.8	3.8	5.5 ± 0.1	18.7 ± 0.5	2.4 ± 0.1	0
6.3	2.5 ± 0.1	12.9 ± 0.3	3.0 ± 0.1	3.8 ± 0.5	4.2	6.9 ± 0.2	20.6 ± 0.7	2.5 ± 0.1	0
16.7	—	—	—	—	4.6	6.2 ± 0.2	16.4 ± 0.6	1.6 ± 0.1	3.0 ± 0.2
37.5	6.8 ± 0.2	17.8 ± 0.4	2.4 ± 0.1	3.6 ± 0.2	2.8	6.9 ± 0.2	16.4 ± 0.5	1.8 ± 0.1	3.2 ± 0.2

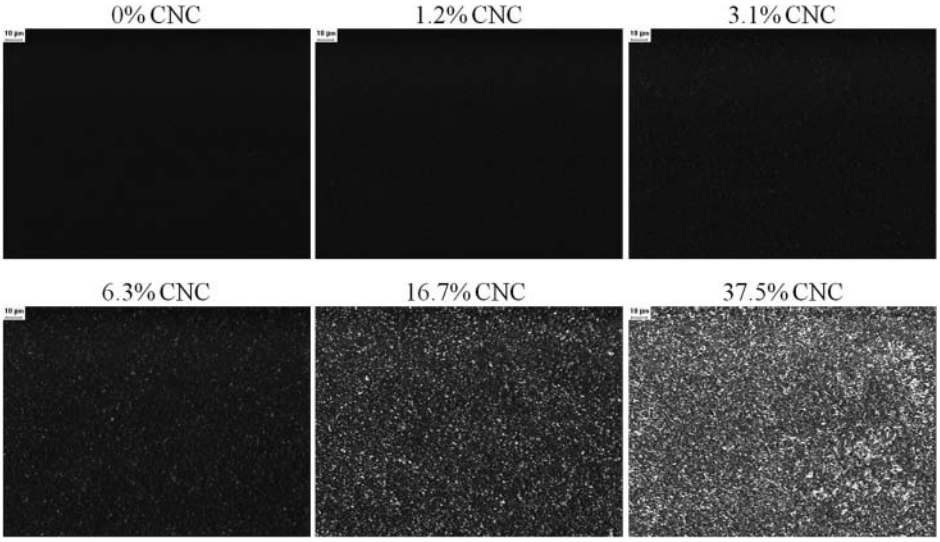

Figure 4. Crossed polarized light microscopy pictures of CNC/sodium alginate films dried from aqueous solutions with 1 wt.% alginate and varying CNC concentrations. The percentages refer to the CNC vol.% in the dried film. Birefringent and non-birefringent domains are visible indicating anisotropic and isotropic regions; a fingerprint texture is starting to form indicating that the preferred orientation is chiral nematic at 37.5% [1].

These findings suggest that the CNCs disrupt the alignment of the alginate chains at low loading, leading to decreased strength. At higher CNC loading, the modulus increases and may be attributed to the formation of a CNC percolation network [21,23] throughout the fiber which yields enhanced strength due to the high modulus of the crystalline cellulose estimated as 143 GPa [24] (equivalent to 988 gpd used later in this work) and greater for an individual CNC [11,25]. Similar behavior has been observed in other CNC nanocomposite materials [11,23,26–32].

Interestingly, the addition of CNCs at low loadings increased the elongation at break and toughness of the fibers. This enables the wet spinning of the nanocomposite fibers at a higher J_A, which leads to an increased rate of fiber production, as well as, enhanced tensile properties. With a 16.7 vol.% CNC load, the maximum J_A achievable with the given fiber spinning system is nearly doubled to a value of 4.6. At a fixed CNC load of 3.1 vol.%

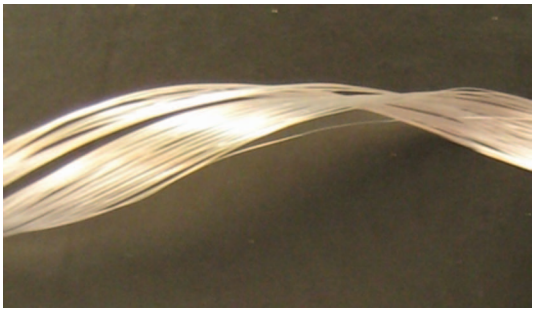

Figure 5. Photograph of CNC – alginate nanocomposite fibers.

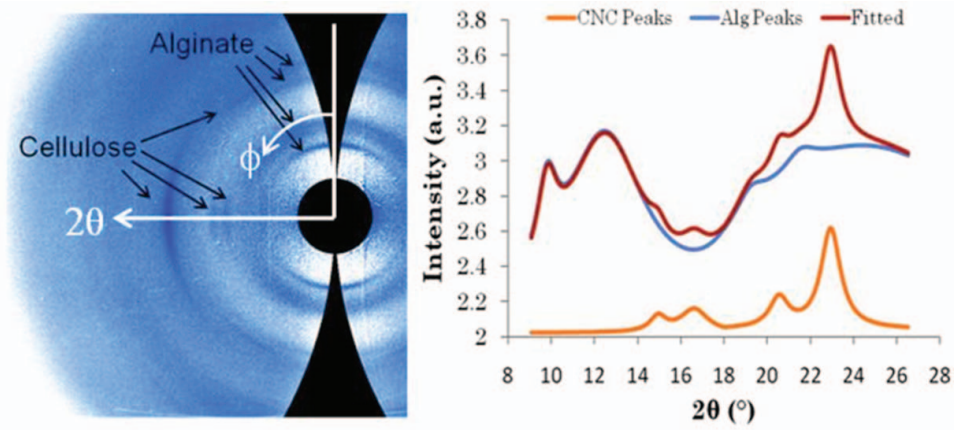

Figure 6. WAXD pattern for a nanocomposite fiber with 6.1 vol.% CNC and $J_A = 2.4$. The scattering for the alginate and cellulose components are denoted as well as the azimuthal angle, (ϕ) and 2θ. The 1-D plot of the intensity averaged with respect to ϕ as a function of 2θ is fit to multiple Lorentzians and deconvoluted to provide independent curves for the alginate and cellulose components.

the modulus and tenacity increase with increasing J_A [1]. Table 1 lists the tensile property enhancements for fibers produced at the maximum J_A achievable for a given CNC load. Expectedly, increased stretching during wet spinning translates into stronger fibers, which can be explained by the extensional flow field forcing the nanoparticles to align along the fiber axis, as well as, increasing the alignment of the alginate polymer chains [2].

It is the inherent nature of the CNCs to twist with respect to one another as evidenced by the cholesteric phase behavior and the chirality present in cellulose fibers [4,13,23,25,27,33]. WAXD is the predominate method to determine the orientation of the crystalline cellulose regions in natural fiber [5,10,11]. Similarly, we have employed WAXD to investigate the impact of CNC load and processing parameters on the molecular level structure within the nanocomposite fibers. Figure 6 is the WAXD diffraction pattern and 1-D diffraction pattern averaged along the azimuthal angle (ϕ) for a 6.3 vol.% CNC fiber spun with a $J_A = 2.4$. The 1-D diffraction patterns were fit to multiple Lorentzians and deconvoluted to extract the CNC and alginate contributions respectively [2]. Analysis of the alginate contributions to the 1-D diffraction confirms that the addition of CNCs does not disrupt the junction zones responsible for the alginate fiber ionic cross linking. Rather, a sharpening and intensification of the diffraction peaks at $2\theta = 9.7^\circ$ and $2\theta = 19.1^\circ$ suggests that the CNC addition induces order within the alginate chains. The CNC contribution to the 1-D diffraction possesses an intense peak at $2\theta = 22.9^\circ$ which corresponds to the (2,0,0) plane reflection within the CNCs. The intensity, $I(2\theta)$, of this peak can be used to determine the CNC volume fraction within fibers of unknown loading. Additionally, this (2,0,0) reflection is used to determine the orientation of the CNCs within the nanocomposite fiber by fitting the intensity as a function azimuthal angle, $I(\phi)$, at $2\theta = 22.9^\circ$ to two Lorentzians of equal width and area. These peaks are symmetric around $\phi = 90^\circ$ and are separated by twice the spiral angle, (2ψ). If the spiral angle is zero, the width of the Lorentzian is proportional to the spread of the crystallites along the fiber axis. If ψ is non-zero, then it is indicative of the spread of CNCs along the spiral orientation.

The measured spiral angles are listed in Table 1. The spiral angle appears to emerge at a critical CNC concentration, however; increased J_A retards the formation of the spiral

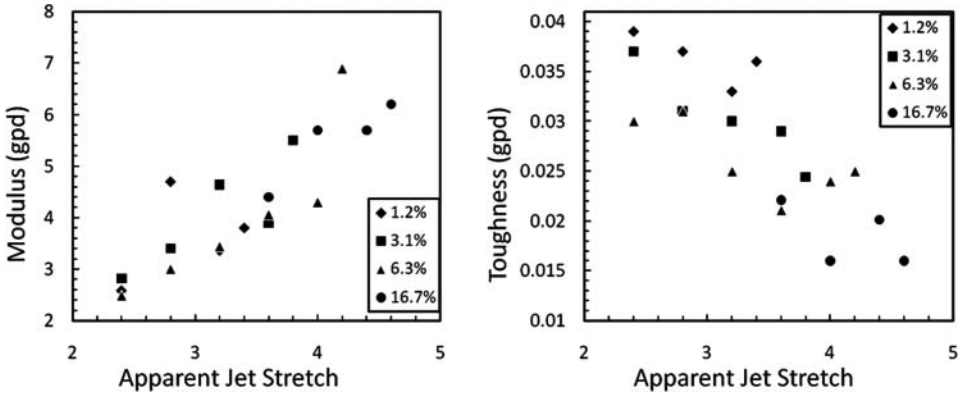

Figure 7. a) Tensile modulus and b) toughness measurements for CNC – alginate nanocomposite fibers as a function of J_A for varying CNC vol.% loading.

structure and promotes alignment along the fiber axis. Interestingly, at max J_A a step decrease in the fiber modulus and tenacity, as well as, a step increases in toughness occurs near the appearance of ψ followed by a continuous increase and decrease respectively. Figure 7 presents the modulus and toughness for the nanocomposite fibers as a function of J_A. For the 1.2 vol.% CNC fibers, a step decrease in modulus is observed at $2.8 < J_A < 3.2$ and a step increase in toughness at $3.2 < J_A < 3.4$. For the 3.1 vol.% CNC fibers, a step decrease in modulus is observed at $3.2 < J_A < 3.6$ and a step increase in toughness is not observed but an s-shaped behavior suggests that a step decrease may exist in this same J_A range. The 6.3 vol.% CNC fibers, a step decrease in modulus is not observed but may exist in the $3.6 < J_A < 4.0$ range where a step increase in toughness is observed. The same is true for the 16.7 vol.% CNC fibers at $4.0 < J_A < 4.4$. We postulate that such discontinuities in the nanocomposite tensile property trends could be the result of the nanoscale structural rearrangements occurring during the disappearance of the spiral assembly as the J_A is increased. Further WAXD measurements of fibers at intermittent J_A's will be required to convincingly elucidate this relationship between spiral angle presence and the resulting tensile properties. Regardless, increasing CNC load promotes the formation of a spiral angle and increased stretching during fiber spinning retards the formation of a spiral angle; each of which impact the resulting tensile properties.

Like any other nanoparticle fillers with an anisotropic geometry, the degree to which CNCs will provide structural reinforcement is largely dependent on the nanofiller orientation within the bulk matrix. In order to understand the fundamental relationship between nanoscale structure and bulk material properties, a number of theoretical approaches have been explored which range from analytical models to molecular dynamics simulations and finite element modeling. In this work, we have employed three analytical models to predict the nanocomposite modulus for a rod-shaped nanofiller with orientations longitudinal (L) and transverse (T) to the strain or fiber direction. The three models applied include the Voigt and Reuss (V-R) model, Halpin-Tsai (H-T) model, and Hui-Shia (H-S) model [34]. The V-R model estimates an upper and lower bound for the nanocomposite modulus, based simply on volume fraction weighting (φ). Equation 1 is used to predict the effective modulus in the nanofiller direction (E_L) where E_f is the nanofiller modulus and E_m is the bulk matrix modulus. For the alginate matrix modulus, $E_m = 3.1$ gpd was measured at $J_A = 2.4$ and used for all models. $E_m = 988$ gpd was calculated from an estimated modulus of 143 GPa

[24]. Equation 2 is used to predict the effective modulus in the transverse direction, normal to the nanofiller direction (E_T). This modeling approach provides a theoretical upper and lower bound for the nanocomposite fiber tensile modulus in the limits that the CNCs would be oriented along the fiber direction and perpendicular to the fiber direction. This simplified model estimates these bounds by volume fraction weighting and inverse volume fraction weighting, depending only on the pure component moduli and volume fractions.

$$E_L = \varphi E_f + (1-\varphi)E_m \tag{1}$$

$$\frac{1}{E_T} = \frac{\varphi}{E_f} + \frac{(1-\varphi)}{E_m} \tag{2}$$

The Halpin-Tsai model [35] is a semi-empirical model based upon the self-consistent micromechanics methods of Hill [36] and Hermans [37]. Equations 3–6 were used to calculate E_L and E_T where α is the nanorod aspect ratio, defined as the rod length to width ratio. For the triaxial CNC nanorods, a geometric mean of the width and height determined by AFM was used for the width component; $\alpha = 11.0$.

$$E_L = \frac{1+2\alpha\varphi\eta_L}{1-\varphi\eta_L}E_m \tag{3}$$

$$\eta_L = \frac{E_f - E_m}{E_f + 2\alpha E_m} \tag{4}$$

$$E_T = \frac{1+2\varphi\eta_T}{1-\varphi\eta_T}E_m \tag{5}$$

$$\eta_T = \frac{E_f - E_m}{E_f + 2E_m} \tag{6}$$

The Hui-Shia model also incorporates the nanofiller aspect ratio in to the E_L and E_T calculations as shown in equations 7–11 [34,38,39].

$$E_L = E_m\left[1 - \frac{\varphi}{\xi}\right]^{-1} \tag{7}$$

$$E_T = E_m\left[1 - \frac{\varphi}{4}\left(\frac{1}{\xi} + \frac{3}{\xi + \wedge}\right)\right]^{-1} \tag{8}$$

$$\xi = \varphi + \frac{E_m}{E_f - E_m} + 3(1-\varphi)\left[\frac{(1-g)\alpha^2 - g/2}{\alpha^2 - 1}\right] \tag{9}$$

$$\Lambda = (1-\varphi)\left[\frac{3\left(\alpha^2 + 0.25\right)g - 2\alpha^2}{\alpha^2 - 1}\right] \tag{10}$$

$$g = \frac{\alpha}{\left(\alpha^2 - 1\right)^{3/2}}\left[\alpha\sqrt{\alpha^2 - 1} - \cosh^{-1}\alpha\right] \quad \text{when } \alpha \geq 1 \tag{11}$$

Figure 8 plots the E_L and E_T predictions for each of the three models and the tensile modulus for the nanocomposite fibers spun at $J_A = 2.4$ and maximum J_A. The longitudinal orientation, E_L, predictions by the V-R model over predict the experimental values but the H-T and H-S models do an excellent job of fitting the modulus for fibers spun at the max. J_A with CNC loads of 1.2, 3.1, and 6.3 vol.%. At higher CNC loading, where a spiral angle

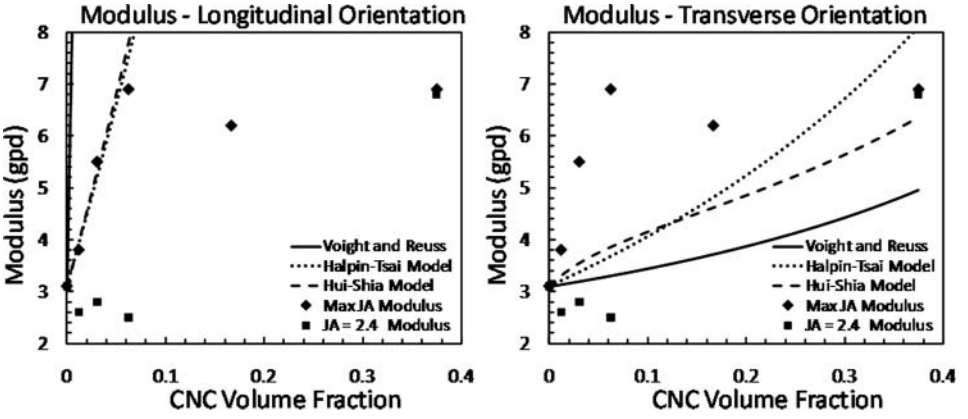

Figure 8. Tensile modulus predictions for nanocomposite fibers with CNCs oriented a) longitudinal and b) transverse to the fiber axis, as compared to experimental measurements for fibers spun at $J_A = 2.4$ and maximum J_A.

is observed for 37.5 vol.% and 16.7 vol.%, the experimental modulus is between the E_L and E_T extremes suggesting an orientation between parallel and perpendicular to the fiber axis. Interestingly, the modulus trends for high CNC loading and for fibers spun at $J_A = 2.4$ are better approximated by the E_T relationships, especially if a lower value of E_m is used for low CNC load. A lower value of E_m may be justified by an induced molecular rearrangement of the alginate chains upon addition of a structure directing agent such as CNC.

Conclusions

Nature's design of cellulosic fibers is undoubtedly remarkable and we have a lot to learn as we aim to translate the nanoscale structure – property relationships found in natural materials to engineered materials. This study provides evidence of an angled orientation of CNCs within an alginate nanocomposite fiber which is achieved above a critical CNC volume fraction and is retarded by fiber stretching during spinning. By altering the CNC nanofiller volume fraction and apparent jet stretch ratio, J_A, during wet spinning the CNC orientation can be altered, which has direct influence on the tensile properties of the nanocomposite fiber. When the fibers are spun at a maximum J_A the CNCs are aligned with the fiber axis and the nanocomposite fiber modulus can be approximated well using the Halpin-Tsai and Hui-Shia semi-empirical analytical models. At low values of J_A, a CNC spiral angle is observed and is likely responsible for discontinuities in the nanocomposite tensile properties observed as a function of CNC load and J_A. This spiral assembly of the CNCs within the nanocomposite is analogous to the well known microfibril angle in natural cellulose fibers and has similar impacts on the fiber tensile properties. This spiral assembly may also be responsible for other unexplained trends in tensile properties for CNC nanocomposites throughout the literature. Future extensions of this work may include the use of CNCs as a renewable, biocompatible nanocomposite additive that can provide structural reinforcement, as well as, increases in toughness. Future applications could range from commercial and consumer products to high-performance self-healing, impact-resistant nanocomposites that rely on nanoscale structural biomimicry.

Acknowledgements

The authors would like to acknowledge the Center for Advanced Engineering Fibers and Films at Clemson University for support and Walter Focke at the University of Pretoria, Republic of South Africa for an invitation to present this work at the 11th International Conference on Frontiers of Polymers and Advanced Materials.

References

[1] Urena-Benavides, E. E., Brown, P. J., & Kitchens, C. L. (2010). *Langmuir*, *26*, 14263.
[2] Urena-Benavides, E. E., & Kitchens, C. L. (2011). *Macromolecules*, *44*, 3478.
[3] Brown, R. M. (2004). *J. Polym. Sci. Part A-Polym. Chem.*, *42*, 487.
[4] Osullivan, A. C. (1997). *Cellulose*, *4*, 173.
[5] Klemm, D., et al. (2002). *Angew. Chem. Int. -Ed.*, *44*, 3358.
[6] Cranston, E. D., & Gray, D. G. (2006). *Biomacromol.*, *7*, 2522.
[7] Gray, D., & Abitbol, T. (2008). *Cellulose Composites Comprising Hydrophobic Particles, Fluorescent Film Intermediate, and their Use in Paper Products*, McGill University: Canada.
[8] Srinivasarao, M. (1999). *Chem. Rev.*, *99*, 1935.
[9] Vukusic, P., & Stavenga, D. G. (2009). *Royal Soc. Interface*, *6*(Suppl. 2), S133.
[10] Barnett, J. R., & Bonham, V. A. (2004). *Biol. Rev.*, *79*, 461.
[11] Eichhorn, S. J., et al. (2001). *J. Mater. Sci.*, *36*, 2107.
[12] Rånby, B. G. (1951). *Discuss Faraday Soc.*, *11*, 158.
[13] Revol, J. F., et al. (1994). *Liq. Cryst.*, *16*, 127.
[14] Beck-Candanedo, S., Roman, M., & Gray, D. G. (2005). *Biomacromol*, *6*, 1048.
[15] Fraser, R. D. B., et al. (1979). *J. Appl. Cryst.*, *9*, 81.
[16] Dong, X. M., et al. (1996). *Langmuir*, *12*, 2076.
[17] Elazzouzi-Hafraoui, S., et al. (2008). *Biomacromol.*, *9*, 57.
[18] Urena-Benavides, E. E., & Kitchens, C. L. (2011). *RSC Adv.*, Submitted.
[19] Dong, X. M., & Gray, D. G. (1997). *Langmuir*, *13*, 2404.
[20] Beck-Candanedo, S., Viet, D., & Gray, D. G. (2006). *Langmuir*, *22*, 8690.
[21] Favier, V., et al. (1997). *Polym. Eng. Sci.*, *37*, 1732.
[22] Wang, Z. H., et al. (2010). *Phys. Chem. Chem. Phys.*, *12*, 3014.
[23] Azizi Samir, M. A. S., Alloin, F., & Dufresne, A. (2005). *Biomacromol.*, *6*, 612.
[24] Sturcova, A., Davies, G. R., & Eichhorn, S. J. (2005). *Biomacromol.*, *6*, 1055.
[25] Samir, M., Alloin, F., & Dufresne, A. (2005). *Biomacromol.*, *6*, 612.
[26] Favier, V., et al. (1995). *Polym. Adv. Technol.*, *6*, 351.
[27] Habibi, Y., Lucia, L. A., & Rojas, O. J. (2010). *Chem. Rev.*, *110*, 3479.
[28] Grunert, M., & Winter, W. T. (2002). *J. Polym. Environ.*, *10*, 27.
[29] Azizi Samir, M. A. S., et al. (2004). *Electrochim. Acta*, *49*, 4667.
[30] Azizi Samir, M. A. S., et al. (2004). *Polymer*, *45*, 4149.
[31] Zimmermann, T., et al. (2006). *ACS Symp. Ser.*, *938*, 33.
[32] Borges, J. P., et al. (2004). *Polym. Compos.*, *25*, 102.
[33] Fleming, K., Gray, D. G., & Matthews, S. (2001). *Chem. -A. Eur. J.*, *7*, 1831.
[34] Hu, H., Onyebueke, L., & Abatan, A. (2010). *J. Miner. Mater. Charac. Eng.*, *9*, 275.
[35] Halpin, J. C., & Kardos, J. L. (1976). *Polym. Eng. Sci.*, *16*, 344.
[36] Hill, R. (1964). *J. Mech. Phys. Solids*, *12*, 199.
[37] Hermans, J. J. (1967). *Koninklijke Nederlandse Akademie Van Weteschappen-Proc. Ser. B-Phys. Sci.*, *70*, 1.
[38] Hui,C. Y., & Shia, D. (1998). *Polym. Eng. Sci.*, *38*, 774.
[39] Shia, D., et al. (1998). *Polym. Compos.*, *19*, 608.